BIOENGINEERING

Single-step label-free nanowell immunoassay accurately quantifies serum stress hormones within minutes

S. Reza Mahmoodi[1], Pengfei Xie[1], Daniel P. Zachs[2], Erik J. Peterson[2], Rachel S. Graham[2], Claire R. W. Kaiser[2], Hubert H. Lim[2], Mark G. Allen[3], Mehdi Javanmard[1]*

A non-faradaic label-free cortisol sensing platform is presented using a nanowell array design, in which the two probe electrodes are integrated within the nanowell structure. Rapid and low volume (≤5 μl) sensing was realized through functionalizing nanoscale volume wells with antibodies and monitoring the real-time binding events. A 28-well plate biochip was built on a glass substrate by sequential deposition, patterning, and etching steps to create a stack nanowell array sensor with an electrode gap of 40 nm. Sensor response for cortisol concentrations between 1 and 15 μg/dl in buffer solution was recorded, and a limit of detection of 0.5 μg/dl was achieved. Last, 65 human serum samples were collected to compare the response from human serum samples with results from the standard enzyme-linked immunosorbent assay (ELISA). These results confirm that nanowell array sensors could be a promising platform for point-of-care testing, where real-time, laboratory-quality diagnostic results are essential.

INTRODUCTION

The precise detection of psychological stress through cortisol level assessment is gaining attention for personalized health monitoring and diagnostics (*1*–*4*). Dysregulation of cortisol has been proposed as a mechanism through which sleep disorders manifest some of their physiologic effects (*5*–*7*). In addition, glucocorticoids can massively fluctuate throughout the day or between treatments (*8*). Therefore, real-time continuous monitoring of cortisol level is more biologically relevant and could be used to quantify the magnitude of the stress in individuals (*9*). However, the conventional cortisol detection approaches such as enzyme-linked immunosorbent assay (ELISA) are restricted to laboratory settings, as they require time-consuming measurements, complex sample preparation, and expensive diagnostic tools (*10*, *11*). A dynamic determination of cortisol in bodily fluids will be an important diagnostic tool to monitor the natural fluctuations of cortisol in daily life without the use of costly and cumbersome laboratory setups (*4*, *12*).

Miniaturized biosensors have shown that using small sample volumes can substantially increase the efficiency, speed, and accuracy of detection (*13*–*16*). Label-free detection can be performed in a single step while also enabling real-time monitoring and determination of the binding kinetics involved in the interaction (*17*, *18*). Among the label-free immunosensing technologies, electrochemical immunosensors have recently emerged as the most promising alternative to optical detection methods due to high sensitivity, ease of miniaturization, and multiparametric analysis (*19*, *20*). These sensors can be integrated into a single-step assay to satisfy the needs of cortisol detection protocols for rapid and selective responses from small sample volumes (*21*).

Multiwell plate testing presents suitable conditions for screening biological or chemical libraries in static fluid environments where multiple samples can be analyzed in parallel (*22*). These platforms can readily be combined with label-free impedance-based biosensors to improve both the sensitivity and efficiency, because it promotes attachment of antibody to the electrode surface and enables simultaneous detection of different analytes by immobilizing their respective ligands on separate electrodes (*23*). Furthermore, non-faradaic impedance biosensors are more amenable to direct applicability for point-of-care diagnostics, as no redox probes or a reference electrode need to be introduced to the sensing scheme (*24*, *25*). However, the sensitivity of this method is generally limited, and interpretation of electrochemical impedance spectroscopy (EIS) data can be difficult, time consuming, and performed in different ways (*26*).

One major drawback of label-free impedimetric immunosensors is that nonspecific bindings and aggregations among the antibody molecules on the electrode surface notably decrease their sensitivity and causes problems in their calibration due to random antibody orientation and subsequent decreased availability of antibody active sites (*27*). Therefore, to fabricate more efficient and reliable biosensors, it is essential to develop a method to immobilize probe antibodies with a more uniform coverage and in a geometric arrangement that minimizes nonspecific bindings. Strategies to overcome this problem involve specific chemistries that limit nonspecific binding, but these approaches do not eliminate nonspecific adsorption entirely (*28*).

The nanowell array biosensors have shown great promise for providing highly sensitive label-free detection by blocking nonspecific bindings without introducing chemical or biological reagents (*27*–*30*). It has also been shown that nanowell array electrodes benefit from rapid detection of biomolecules with higher reproducibility, because these sensors can reduce mass transfer limitations (*31*, *32*). However, in many of these systems, the counter electrodes are separated by either a large spacing or a distance that is in the same range as for the common interdigitated electrodes, typically in the range of 2 to 10 μm. Furthermore, the generation of strong electrical field is a requirement for developing highly sensitive sensors and is achievable by keeping the electrodes close together (*33*). Moreover, it has been shown that AC signal can accelerate the

[1]Rutgers University, Piscataway, NJ 08854, USA. [2]University of Minnesota, Minneapolis, MN 55455, USA. [3]University of Pennsylvania, Philadelphia, PA 19104, USA.
*Corresponding author. Email: mehdi.javanmard@rutgers.edu

incubation process and enhance the immunosensor sensitivity by encouraging macromolecule binding (*34*, *35*).

This study presents a nanowell array design, in which the electrodes are stacked vertically above one another to minimize the electrode spacing. The electrodes are separated by a 40-nm insulator layer within the nanowells; thereby, the counter electrodes are integrated into the nanowell structure. Numerical simulation of the electric field generation inside the nanowells is shown in fig. S1. This sensor geometry limits the exposed surface area of the electrodes, and, as a result, the amount of probe antibody molecules inside the nanowells, while also enhancing the sensitivity by focusing the electric field into the nanowells. The nanogap distancing reduces the noise from electrode polarization effects and solution conductivity, thereby producing a more accurate signal (*36*, *37*). Figure 1A presents a schematic for multiplex testing using multiwell plate platform, i.e., measuring multiple analytes at the same time for rapid label-free biosensing in small volumes. In this study, the nanowell array electrodes were used to immobilize probe antibodies inside the nanowells while applying AC signal. The biosensor yielded a limit of detection of 0.5 μg/dl in buffer solution, and the sensor specificity was tested against negative controls. The functionalized sensor is then used to measure cortisol levels in human serum by real-time impedance monitoring. The chip contains 28 pairs of sensors that can be functionalized with various types of receptors for the ultimate goal of multiplexed point-of-care testing.

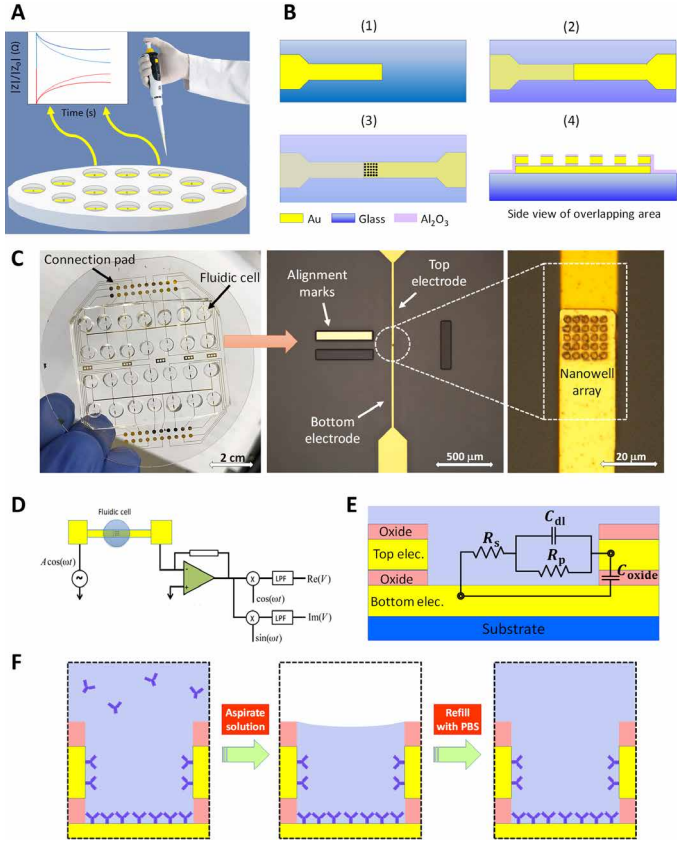

Fig. 1. Preparation and testing procedure of nanowell array sensor. (**A**) Schematic for multiplex testing, i.e., a biosensor chip based on impedance detection to monitor multiple analytes in real time. (**B**) Fabrication steps of the nanowell array sensor. Top view of (1) patterning bottom electrode, (2) ALD of interelectrode aluminum oxide layer and patterning top electrode, (3) ALD of protective layer aluminum oxide and ion milling etching to create nanowell arrays, and (4) side view of nanowell array on the overlapping electrodes. (**C**) A 28-well plate chip produced after PDMS bonding and microscopic images of the electrodes at low and high magnifications, respectively, showing the formation of an array of 25 nanowells on the overlapping electrode surface. Photo credit: Seyed Reza Mahmoodi, Rutgers University, (**D**) Measurement setup using lock-in amplifier. (**E**) Equivalent circuit model fitted to the experimental data. (**F**) After incubation, the liquid over the nanowells was aspirated to minimize any nonspecific adsorption and PBS was reinjected. LPF, Low Pass Filter.

RESULTS AND DISCUSSION

EIS tests were carried out on bare electrodes immersed in different media before real-time impedance measurements. The EIS spectra in air, deionized (DI) water, and purified buffer with three different concentrations are shown in Fig. 2A. In air, because there is no solution present inside of the nanowells, the impedance spectrum can be simplified to be expressed by a constant C_{oxide} over the entire frequency range. The fitted value for C_{oxide}($\approx 1.88 \times 10^{-3}$ nF) correlates well with the estimated capacitance of the electrode pair $\left(c = \frac{\varepsilon\varepsilon_0 \times A}{d}\right)$, which is calculated to be around $C_{oxide} \approx 1.19 \times 10^{-3}$ nF, where $\varepsilon_{oxide} = 16.7\ \varepsilon_0$, $A_{oxide} = 321.46\ \mu m^2$, and $d_{oxide} = 40$ nm. Moreover, comparing the EIS spectra of air with different media shows that the capacitive contribution of the oxide layer is quite negligible. Therefore, C_{oxide} can be disregarded in the sensor circuit fitting when DI water or a buffer is present inside the nanowells. The 10× buffer shows a flat impedance response at lower frequencies and undergoes a transition from about 10 kHz onward. On the contrary, the more diluted buffers of 5× and 1× phosphate-buffered saline (PBS) show more broad range of impedance variations with regard to frequency, and the spectra flatten out beyond 500 and 100 kHz, respectively.

In Fig. 2B, the impedance spectra of 1× PBS are more detailed by measuring the phase angle and the real (Real Z) and imaginary part (Imag Z) of impedance. As shown, the impedance transition at around 100 kHz happens when the Real Z value becomes larger than the absolute value of Imag Z and the impedance phase plot also identifies that the resistance dominates the impedance response above ~200 kHz. Similarly, for DI water response show in Fig. 2A, the absolute value of impedance is dominated by Real Z at frequencies beyond ~5 kHz. Figure 2C shows the real-time impedance measurement of bare electrodes when an empty test cell is filled with 20 μl of 1× PBS at four different frequencies. By increasing the frequency, the impedance value after immersion tends to a constant level, and the initial baseline shift in the impedance decreases. This is in agreement with the obtained EIS results in Fig. 2A. Here, to avoid the inductive effect in the system at high frequencies, we chose to operate at 1 MHz in 1× buffer solution.

In the next step, the nanowell array electrodes were functionalized with cortisol antibody, while the impedance across the electrodes was monitored in real time. As shown in Fig. 2D, by the introduction of antibody solution, the Real Z plot remains nearly constant throughout the measurement, while the Imag Z plot shows a curved increase over time after an immediate baseline shift. Therefore, the variations of Imag Z plot during the antibody immobilization directly affect the total impedance plot. The minor baseline shift in the Real Z plot can be because the fluid injection does not change the bulk solution resistance as both anti-cortisol and cortisol are diluted in the same buffer. Hence, the real-time impedance measurement at

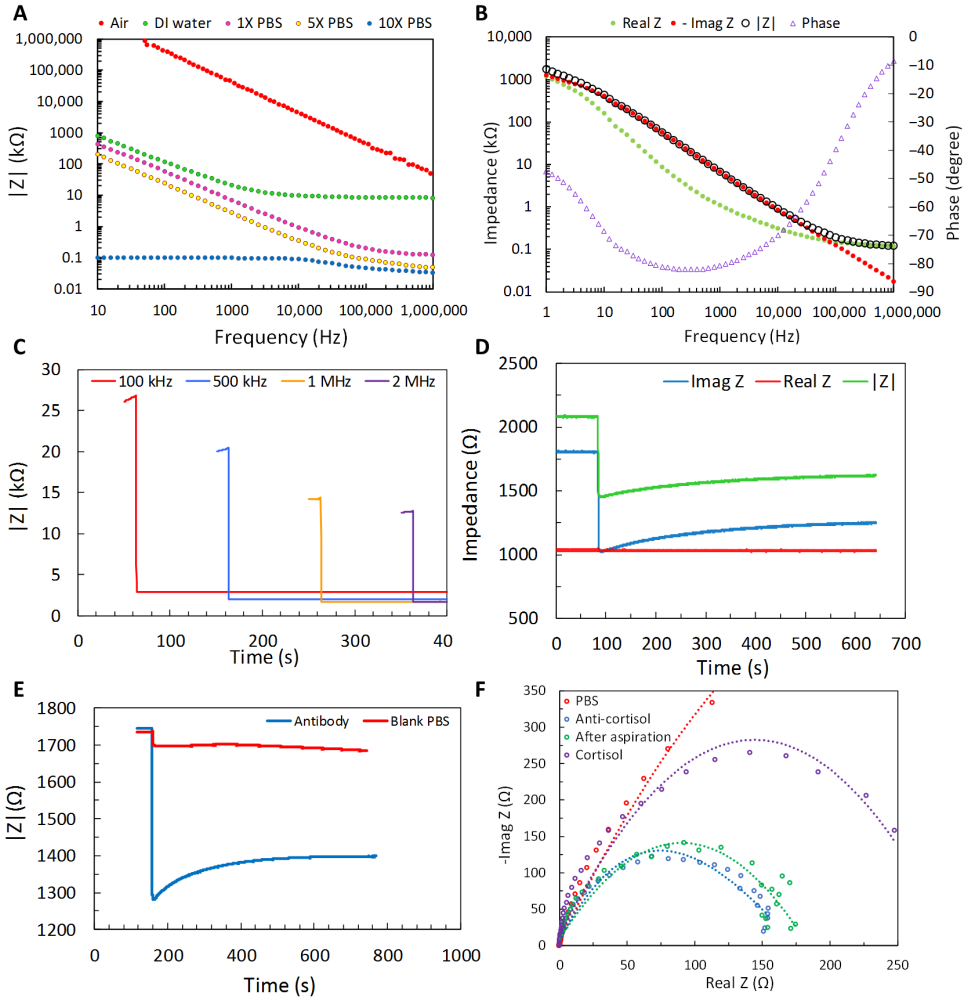

Fig. 2. Impedance characterization of nanowell array electrodes. (**A**) EIS spectra of nanowell array electrodes measured in different media. (**B**) EIS characteristic of nanowell array electrodes in 1× PBS. (**C**) Real-time impedance monitoring of impedance at four different frequencies by the immersion in 1× PBS. (**D**) Real-time monitoring of cortisol antibody immobilization for an incubation time of around 10 min. (**E**) Comparison of real-time monitoring of impedance after injection of blank PBS (red, before functionalization of the sensor) and anti-cortisol immobilization curve (blue). (**F**) EIS measurement in the form of Nyquist plot for pure PBS after antibody immobilization and after solution aspiration.

high frequencies allows to separate the parasitic effect of the bulk resistance from the sensor response. The real-time impedance monitoring of anti-cortisol immobilization is also compared with blank PBS addition to the bare electrodes in Fig. 2E. Before antibody immobilization, a blank PBS sample was added to the cell, resulting only in a minimal shift in the baseline. The anti-cortisol plot shows a more pronounced baseline shift followed by a characteristic capacitive curve to reach a plateau.

The EIS spectra of antibody immobilization are presented in Fig. 2F to confirm the subsequent binding of cortisol antibody during the sensor functionalization step in the nanowells. As illustrated in Fig. 1E, after the immobilization step, the fluid in the cell was aspirated and PBS was reinjected to avoid sensor fouling. At bare nanowell electrodes, a straight line could be observed, indicating a low polarization resistance (PBS curve). Nyquist plot after aspiration remains mostly identical to the plot before aspiration, confirming attachment of anti-cortisol inside the nanowells after aspiration and refilling with PBS. The cortisol plot in Fig. 2F also displays the EIS response to a dose of cortisol (5 μg/dl). The increased diameter of semicircle after immunoreaction implies the formation of immune complex by changing the polarization properties of the nanowells.

In the real-time experiments, impedance is normalized on the basis of its initial value immediately after the baseline shift and converted to capacitance using the Imag Z plot to record the relative changes of both parameters. The sensor response was then quantified by measuring the difference between the impedance immediately after the shift and the final impedance magnitude. The normalized impedance and capacitance plots in separate experiments are shown in Fig. 3 to examine the sensor behavior toward different stimuli. During the antibody incubation, shown in Fig. 3A, the initial baseline shift can be associated with the immediate changes in the medium properties. However, the characteristic time-dependent rise in impedance (or decrease in capacitance) is consistent with antibody immobilization in the nanowells due to the decrease in dielectric polarization and, therefore, indicates the successful modification of the nanowell surface.

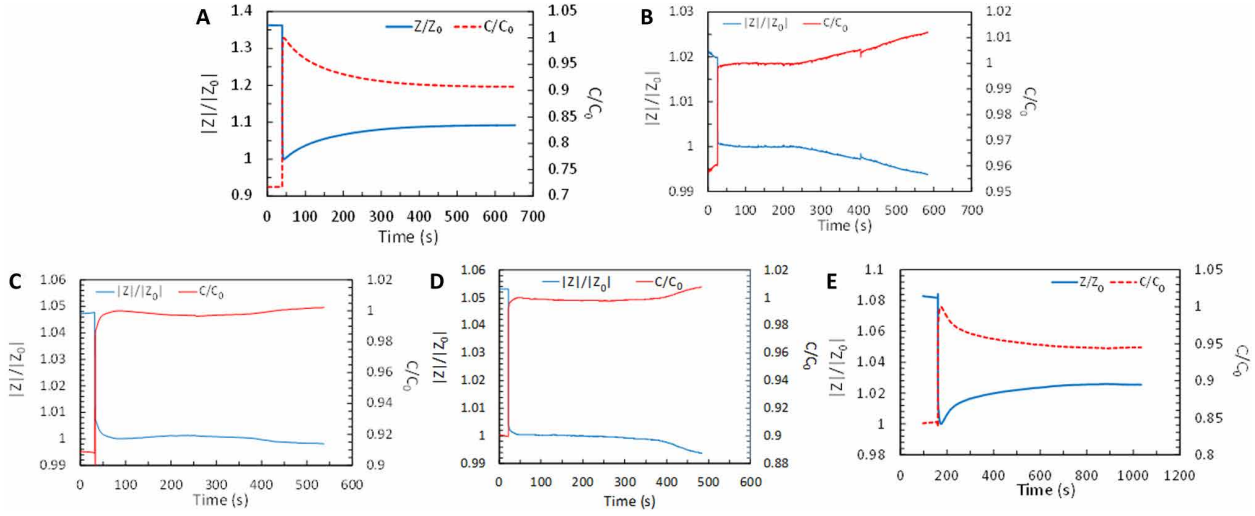

Fig. 3. Illustration of experimental protocol for device validation and resulting changes in normalized impedance and capacitance. (**A**) Antibody immobilization. Negative control steps: (**B**) adding blank samples does not effectively affect the impedance, (**C**) nontargeted IL-6 remains almost constant after the baseline shift, and (**D**) nontargeted testosterone results in a small decrease in impedance or increase in capacitance after the baseline shift. All negative controls do not show specific binding trend. (**E**) Cortisol specific binding (3 μg/dl) results in an increase in impedance or a decrease in capacitance after the baseline shift, similar to antibody adsorption.

After antibody immobilization, real-time testing was conducted to study the normalized sensor response to positive and negative controls, as illustrated in Fig. 3 (B and E). Negative controls of blank PBS and PBS spiked with interleukin-6 (IL-6) and testosterone were used to show the selective response of the sensor. We used IL-6 and testosterone as negative controls because these ligands are biologically or structurally relevant (*3*) and it is known that IL-6 is able to induce an increase in plasma cortisol (*38*). In the case of negative control PBS shown in Fig. 3B, the insertion creates only a small shift in the baseline followed by a negligible decrease in the impedance. For nontarget analytes, IL-6 and testosterone, the impedance undergoes a more pronounced baseline shift and remains nearly constant thereafter (Fig. 3, C and D). Figure 3E shows that the addition of cortisol results in a curved rise in impedance after the baseline shift, with a signature similar to that observed during antibody immobilization. Unlike the negative control responses, cortisol spiked sample results in a positive change in impedance after the baseline shift due to the gradual drop in the capacitive properties of the nanowells. This confirms the effective formation of an immune complex between cortisol and antibody. The baseline shift in capacitance stems from the movement of free ions to or from the electrode interface, which immediately modifies the nanowell dielectric polarization. However, the target biomolecule binding, in the form of a time-dependent curve, produces a quantifiable variation in the capacitive characteristics between the electrodes that can be associated with cortisol binding.

As shown in fig. S2, the normalized impedance shows correlation with the applied potential during the antibody immobilization step. The response curve rises by the increase in voltage and reaches to maximum at 200 mV. Recently, AC electric field has found use in capturing, alignment, and enhanced detection of biomolecules (*34*, *39*). The electric field entrapment has previously been combined with the antigen-antibody reaction to facilitate selective detection, and it has been used to immobilize antibody probe (*40*–*42*). Here, in fig. S2, although a definitive explanation of this result awaits further testing, we hypothesize that when the applied voltage is very small, electric forces cannot inhibit random antibody immobilization, which diminishes the positive response curve. Moreover, the high electric field strength inside the nanowells can potentially enhance the sensor performance by encouraging uniform attachment and specifically orienting antibodies along the electric field lines.

To further validate the sensor readings, a titration experiment was designed to determine the sensor response to samples with cortisol (1.5, 3, 5, 7, 10, and 15 μg/dl) in purified buffer. The normalized impedance monitoring plots in Fig. 4A show how the response changes after the baseline shift with increasing dosage of cortisol. As cortisol concentration increases, the cortisol-antibody binding decreases the capacitive charging (C_{dl}) between the electrodes, which causes an increased shift in the impedance plots in Fig. 4A. Figure 4B shows the calibration plot of the biosensor with respect to cortisol concentration. As shown in Fig. 4B, the sensor shows a linear response toward cortisol concentration with a correlation coefficient (R^2) of 0.94. In the lower limit of 1.5 μg/dl, the characteristic shift of impedance becomes more flat, like negative control responses. Using the standard method reported in the literature (*43*), the detection limit for the immunosensor was calculated to be about 0.5 μg/dl in PBS buffer. A comparison of several representative studies on electric-based immunosensors is provided in table S1. In the following experiments, the ability of the array nanosensor to quantify cortisol levels in human serum samples is emphasized when benchmarked against the gold standard ELISA. Although the obtained detection limit is slightly higher when compared with the other studies, the results from human serum samples approve that the fabricated assay can reliably be used at a single frequency to detect cortisol in a normal range of cortisol in human serum (~5 to 25 μg/dl).

To showcase the agnostic nature of the platform technology and its utility in human serum matrix, we calibrated the nanowell sensor based on human serum samples. The obtained results were validated with ELISA technique to estimate cortisol concentration in human serum samples. For this reason, a standard cortisol ELISA test was conducted on 65 different human serum [healthy and rheumatoid arthritis (RA) patient] samples (5 μl). The sensor behavior toward healthy human serum (~5 μg/dl) is shown in Fig. 5A. As

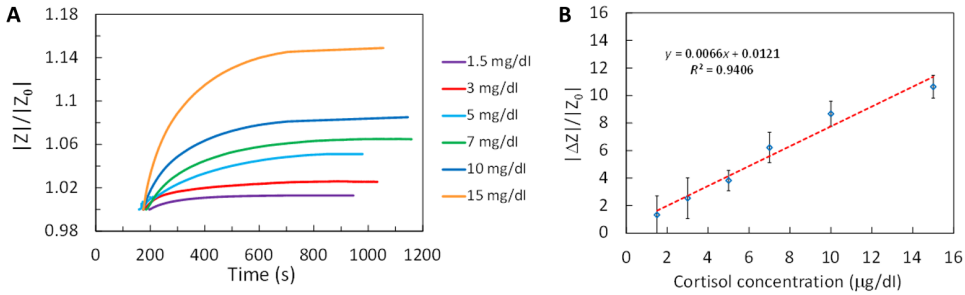

Fig. 4. Sensor calibration in PBS buffer. (**A**) Sensor response to different doses of cortisol spiked in PBS buffer solution. (**B**) Corresponding calibration curve of cortisol detection based on the changes in the normalized impedance after the baseline shift.

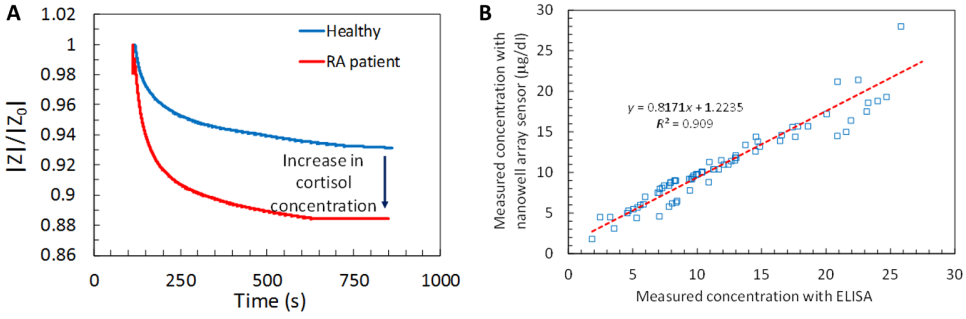

Fig. 5. Sensor calibration of human serum samples. (**A**) Relative changes in impedance for human serum samples (RA patient and healthy control samples). (**B**) Comparison of the cortisol concentration results with the results obtained by standard ELISA method from 65 human serum samples.

shown in Fig. 5A and fig. S3, unlike cortisol spiked buffer samples, serum injection increases the baseline because of introduction of a high concentration of biomolecules into the open fluidic well, which instantly modifies the medium conductivity and dielectric properties. In Fig. 5A, the time-dependent drop is minimal for healthy control samples, and by increasing the cortisol dosage in RA patient samples, the curve (drop in impedance) becomes larger. In serum tests, similar to the purified buffer samples, the increase in specific binding results in a larger change in impedance, however, given the nature of the matrix, the sensor experiences a decrease in impedance (increase in capacitance). The results approve that the nanowell array sensor is capable of cortisol detection regardless of the salt concentration of the medium.

The cortisol concentration obtained using ELISA was compared with the values measured by the nanowell array sensor in Fig. 5B. The linear regression equation shows a slope of 0.82 with a regression coefficient of 0.91. The obtained results approve the sensing performance of the nanowell immunosensor despite the small deviation from ideal slope of one. In a practical setting, a single step involving sample injection would be sufficient to perform sample-to-answer analysis using the nanowell sensor within 10 min. This ease of use can enable a plethora of applications ranging from medical diagnostics to environmental monitoring and food safety.

Conclusion and Outlook

This study presents a sensing platform, the nanowell array sensor, that is formed by vertical stacking of electrodes to minimize the interelectrode spacing without imposing costly manufacturing procedures. We present a non-faradaic real-time impedimetric biosensor to detect cortisol in human serum in small volumes in the range of 2 to 5 µl. EIS characterization was performed in different media to optimize the frequency limit for the real-time impedance measurements. The sensor's specificity to cortisol was achieved through functionalized nanowells with cortisol antibody as the active sensing element. Binding of target cortisol modulates the impedance after the instant baseline shift, resulting in a characteristic change in impedance due to modulation of capacitive charging between the two electrodes inside the nanowells. As a result, we were able to reliably and repeatedly detect both target cortisol spiked in PBS buffer at concentrations as low as 1.5 µg/dl and also endogenous levels of cortisol in human serum samples within 10 minutes. Sensor specificity was established through testing with blank PBS, IL-6, and testosterone. ELISA test was carried out to detect cortisol concentration in 65 human serum samples to compare with the results obtained from the nanowell array sensor at a single frequency. The performance was validated with conventional ELISA method and exhibited a remarkable correlation.

This study aims to bring laboratory-quality diagnostic to point of care and patient self-testing at a lower cost, and cortisol was chosen as a model analyte. The primary challenge faced by label-free technologies stems from measurement inconsistency, thus not being suitable for reliable quantification of molecular levels. The array structure of the sensor increases the probability of diffusion of the analyte and its subsequent binding to the sensor active area. Moreover, the sensor platform concentrates the electric field into the small volume of wells and reduces the noise from electrode polarization effect and solution conductivity, thereby producing a more accurate and reliable response. These systems can allow a continuous readout of cortisol levels for real-time analysis of patients subjected to stress and have great potential to be adapted to noninvasive

cortisol measurement in desired biofluids such as human saliva and urine.

MATERIALS AND METHODS

Sensor fabrication

The fabrication steps of the stack electrodes are demonstrated in Fig. 1B. Fused silica substrate (UniversityWafer, MA, USA) was treated by oxygen plasma for 2 min to clean the surface. The metal electrode consists of a 5-nm layer of chromium for enhancing adhesion of the gold film to the substrate, a 150-nm gold layer, and a 5-nm aluminum layer. The chromium and gold layers were deposited by electron beam evaporation followed by sputtering the aluminum top layer. After successive deposition of different metal layers, the bottom electrode was patterned by liftoff (step 1). The aluminum surface oxidizes in atmosphere to enhance the adhesion between the metal electrode to the next oxide layer. A 40-nm layer of aluminum oxide was then deposited on top of the first electrode using atomic layer deposition (ALD). The ALD process was performed in plasma-assisted mode at 250°C. The second electrode layer (again consisting of 5-nm chromium, 150-nm gold, and 5-nm aluminum) was patterned using the same procedure as the first layer (step 2). Another 40-nm layer of aluminum oxide was deposited on top of the second electrode using ALD. The protective oxide layer limits the active surface area of the electrodes in a way that the gold electrode is only exposed to the testing fluid through the nanowells. This can reduce nonspecific binding and enhance electrochemical responses by selective docking of single molecules and controlling the amount of probe antibodies. Subsequently, a layer of resist was spin-coated onto the wafer to photo-pattern an array of micrometer-sized holes onto the overlapping surface of the electrode stack. The ion milling process was performed to drill holes from the top oxide surface all the way down to the bottom gold electrode. The photoresist was then stripped off (step 3 and side view is shown in step 4). All electrode connection pads were protected by Kapton tape during the entire fabrication procedure.

In the overlapping area (20 μm by 20 μm), the two electrodes were separated by a thin aluminum oxide insulating layer to create an electric path via the test solution inside the nanowells. Connection pads were fabricated on opposing sides of the chip with traces leading to the center of the chip. Open fluidic wells, for confining the liquid, made of polydimethylsiloxane (PDMS) were then bonded on top of the sensor substrate by oxygen plasma treatment. The plasma treatment also cleans off the residues from the nanowells before testing. The diameter of each open fluidic well is 5 mm, which allows fluid to be directly incubated onto individual sensors. Therefore, a 28-well plate chip is formed by bonding the PDMS on the glass wafer, which can be used for detection of different biomarkers in parallel experiments. Figure 1C shows the PDMS-bonded chip of electrodes, including two zoomed-in micrographs from an individual electrode pair and the overlapping region of two gold electrodes to demonstrate the formation of an array of 2-μm wells.

In terms of design considerations, the smaller interelectrode spacing moderates the electrode polarization effect, which results in higher electric field density, and thus enhances sensitivity toward biomolecular interactions. On the other hand, lowering the thickness of the insulating layer leads to smaller gap length between the electrodes, which can cause nonuniform current distribution between the nanowells in an array electrode design. Therefore, the gap length should be high enough to endow the array structure high controllability and reproducibility. Accordingly, we tested devices with oxide thicknesses of 30 and 40 nm to determine which provides better sensitivity. Devices with 40-nm spacing showed larger change in normalized response when antibody physically adsorbed inside the nanowells compared to devices with 30-nm spacing. Because the 40-nm thickness provided a strong response, probably in effect of a more uniform current distribution, further testing was performed using 40-nm-thick oxide devices with 2-μm-diameter wells.

Impedance characterization

It is critical to understand the impedance response of the system to determine the optimum frequency region for performing real-time measurements. We used a potentiostat (Gamry Instruments, Warminster, PA, USA) to characterize the impedance spectrum of the sensor in a two-electrode configuration. First, the devices were tested in air, DI water, 10× PBS, diluted 5× PBS, and 1× PBS to analyze the sensor characteristics in different media. Non-faradaic EIS spectra were recorded in a range from 100 Hz to 1 MHz at 10-mV signal. For sensor characterization tests, 1× PBS was used as the medium buffer. Before introducing PBS onto the device, the wells were washed with ethanol and DI water and then washed three times with PBS. From the EIS spectra, we observed that the real-time impedance shift over time can be influenced by both capacitance and resistance. As a result, sensing is accomplished through monitoring changes in absolute impedance and capacitive charging of the system at 1 MHz.

Reagents were sequentially added manually to the well, and the complex impedance data were monitored in real time. Sensors were isolated from external electromagnetic interference using a Faraday cage, reducing external interference and allowing reliable measurements. A lock-in amplifier (HF2IS-MF multifrequency; Zurich Instruments, Zurich, Switzerland) was used to apply voltage and monitor the absolute impedance ($|Z|$) across the electrodes to continuously improve on signal-to-noise ratio during the data acquisition time. $|Z|$ reflects the total impedance of the system and can be used as a measure of both capacitive and resistance changes. Figure 1D shows a schematic describing the test setup. The AC excitation source, providing 400 mV at a frequency of 1 MHz, was connected to one of the electrodes, and the second electrode was connected to the input of the lock-in amplifier, where the real and imaginary components of the impedance were both acquired. The output voltage of the lock-in amplifier was converted to impedance using $Z = \frac{V_{in} \cdot G}{V_{out}}$. Figure 1E presents the circuit model used to analyze the impedance results. The listed components include solution resistance (R_s), polarization resistance (R_p), and double-layer capacitance (C_{dl}). In each set of experiments, the impedance measurements were started in 20 μl of PBS. Then, by small additions of PBS (~2 μl) to the bare electrodes, the impedance stability was checked to ensure that the response reaches a plateau after around 10 min. The obtained impedance data were converted to capacitance values using $C = -\left(\frac{1}{\omega Z''}\right)$, where C is the capacitance, ω is the angular frequency, and Z'' is the imaginary part of the impedance. The devices were calibrated by plotting the value of $\left(\frac{Z}{Z_0}\right)$ as a function of the cortisol concentration in solution. Continuous impedance monitoring at high frequency of 1 MHz allows to discriminate between the parasitic effect of the buffer solution from the impedance changes due to modulation of the capacitance between the electrodes.

Reagent preparation and antibody immobilization

Antibody and target cortisol were suspended in 1× PBS. Anti-cortisol antibody (ab1952, Abcam) was suspended in PBS at a concentration of 0.2 mg/ml. The target cortisol hormone (Cortisol-BSA, 80-1434, Fitzgerald) was diluted to reach concentrations ranging from 1.5 to 15 μg/dl. For negative control experiments, we used blank PBS and PBS spiked with human IL-6 protein (206-IL, R&D Systems) and testosterone hormone (Testosterone-BSA, 80-1064, Fitzgerald), because the target cortisol was diluted in PBS. For determining the calibration curve, the target cortisol solution was further diluted with PBS at various ratios to inject a similar volume of buffer (5 μl) onto the cell. The probe antibody was immobilized onto the sensor surface by injecting anti-cortisol solution (5 μl) into the sensor cell and incubating for 15 min while applying AC signal to speed up the binding processes (*34*, *44*). Before sensor characterization, the fluid in the PDMS cell was aspirated to remove remaining antibodies in the solution to prevent any nonspecific adsorption, and PBS was reinjected (Fig. 1F). As shown in Fig. 1F, multilayer stacking of the sensor increases the height of the electrode overlapping area compared to its surrounding, which allows to aspirate the sensor while the fluid remains inside the nanowells by capillary attraction. Therefore, the aspiration process confines probe attachment to the nanowell volume by washing away antibodies that are attached outside the nanowells and nonbinding antibodies in the solution.

We measured the cortisol dosage in human serum to test the effects of the background matrix on the sensor. Therefore, similar to the aforementioned procedure, the nanowell sensor responses were calibrated on the basis of human serum samples collected from volunteers and the results were compared with response from commercial (healthy) human serum (Sigma-Aldrich, USA). Cortisol concentrations in 65 human serum samples (RA patient) were quantified by the Human Cortisol ELISA Kit (Biotang Inc.). Samples from RA patients were obtained from patients with a varied range of inflammatory status. Patients were selected with a diagnosis of seropositive RA (rheumatoid factor positive or cyclic citrullinated peptide antibody positive) and symptoms or signs of inadequate disease control. Both male and female patients were selected between the ages of 33 and 89 years at time of collection. Patients were excluded if they had active bacterial or viral infection, pregnancy, or malignancy. These patients were part of an ongoing clinical trial for the treatment of RA (further details of the clinical study are available on clinicaltrials.gov NCT03690466). A titration curve was then extracted from testing the first 20 human serum samples based on the ELISA results. The concentrations of cortisol in the next 45 samples were calculated according to the obtained titration curve. A linear correlation factor was obtained as a measure of consistency of the nanowell sensor response compared to ELISA. In serum experiments, undiluted sera were added to the open fluidic wells that were filled with 20 μl of PBS buffer. Therefore, the serum samples were diluted with the buffer solution. All serum samples were stored at −20°C to maintain their biological activity. All the samples were brought to room temperature for further use to detect cortisol concentration using nanowell immunosensors and ELISA.

SUPPLEMENTARY MATERIALS

Supplementary material for this article is available at http://advances.sciencemag.org/cgi/content/full/7/27/eabf4401/DC1

View/request a protocol for this paper from *Bio-protocol*.

REFERENCES AND NOTES

1. A. Kaushik, A. Vasudev, S. K. Arya, S. K. Pasha, S. Bhansali, Recent advances in cortisol sensing technologies for point-of-care application. *Biosens. Bioelectron.* **53**, 499–512 (2014).
2. A. K. Sahi, N. Varshney, R. K. Sidu, S. Poddar, Pallawi, K. Singh, S. K. Mahto, Clinical implications of cortisol and bioanalytical methods for their determination in various biological matrices, in *Immunodiagnostic Technologies from Laboratory to Point-of-Care Testing*, P. Suman, P. Chandra, Eds. (Springer, 2020), pp. 195–221.
3. A. E. Taylor, B. Keevil, I. T. Huhtaniemi, Mass spectrometry and immunoassay: How to measure steroid hormones today and tomorrow. *Eur. J. Endocrinol.* **173**, D1–D12 (2015).
4. M. Sekar, R. Sriramprabha, P. K. Sekhar, S. Bhansali, N. Ponpandian, M. Pandiaraj, C. Viswanathan, Review—Towards wearable sensor platforms for the electrochemical detection of cortisol. *J. Electrochem. Soc.* **167**, 067508 (2020).
5. L. M. Tomfohr, K. M. Edwards, J. E. Dimsdale, Is obstructive sleep apnea associated with cortisol levels? A systematic review of the research evidence. *Sleep Med. Rev.* **16**, 243–249 (2012).
6. L. Palagini, C. H. Bastien, D. Marazziti, J. G. Ellis, D. Riemann, The key role of insomnia and sleep loss in the dysregulation of multiple systems involved in mood disorders: A proposed model. *J. Sleep Res.* **28**, e12841 (2019).
7. J. Labad, A. Stojanovic-Pérez, I. Montalvo, M. Solé, Á. Cabezas, L. Ortega, I. Moreno, E. Vilella, L. Martorell, R. M. Reynolds, A. Gutiérrez-Zotes, Stress biomarkers as predictors of transition to psychosis in at-risk mental states: Roles for cortisol, prolactin and albumin. *J. Psychiatr. Res.* **60**, 163–169 (2015).
8. J. Obleser, J. Kreitewolf, R. Vielhauer, F. Lindner, C. David, H. Oster, S. Tune, Circadian fluctuations in glucocorticoid level predict perceptual discrimination sensitivity. *iScience* **24**, 102345 (2021).
9. P. J. Taylor, C. H. Thompson, N. D. Luscombe-Marsh, T. P. Wycherley, G. Wittert, G. D. Brinkworth, Efficacy of real-time continuous glucose monitoring to improve effects of a prescriptive lifestyle intervention in type 2 diabetes: A pilot study. *Diabetes Ther.* **10**, 509–522 (2019).
10. D. Kinnamon, R. Ghanta, K.-C. Lin, S. Muthukumar, S. Prasad, Portable biosensor for monitoring cortisol in low-volume perspired human sweat. *Sci. Rep.* **7**, 13312 (2017).
11. S. T. Sanjay, M. Li, W. Zhou, X. Li, X. J. Li, A reusable PMMA/paper hybrid plug-and-play microfluidic device for an ultrasensitive immunoassay with a wide dynamic range. *Microsyst. Nanoeng.* **6**, 28 (2020).
12. Y. Hwang, N. K. Gupta, Y. R. Ojha, B. D. Cameron, *Nanoscale Imaging, Sensing, and Actuation for Biomedical Applications XIII* (International Society for Optics and Photonics, 2016), vol. 9721.
13. J. Wang, Electrochemical biosensors: Towards point-of-care cancer diagnostics. *Biosens. Bioelectron.* **21**, 1887–1892 (2006).
14. L. Soleymani, F. Li, Mechanistic challenges and advantages of biosensor miniaturization into the nanoscale. *ACS Sensors* **2**, 458–467 (2017).
15. Z. Liao, J. Wang, P. Zhang, Y. Zhang, Y. Miao, S. Gao, Y. Deng, L. Geng, Recent advances in microfluidic chip integrated electronic biosensors for multiplexed detection. *Biosens. Bioelectron.* **121**, 272–280 (2018).
16. J. Kim, A. S. Campbell, B. E. F. de Ávila, J. Wang, Wearable biosensors for healthcare monitoring. *Nat. Biotechnol.* **37**, 389–406 (2019).
17. A. Syahir, K. Usui, K. Tomizaki, K. Kajikawa, H. Mihara, Label and label-free detection techniques for protein microarrays. *Microarrays* **4**, 228–244 (2015).
18. X. Yu, D. Xu, Q. Cheng, Label-free detection methods for protein microarrays. *Proteomics* **6**, 5493–5503 (2006).
19. A. Singh, A. Kaushik, R. Kumar, M. Nair, S. Bhansali, Electrochemical sensing of cortisol: A recent update. *Appl. Biochem. Biotechnol.* **174**, 1115–1126 (2014).
20. P. Xie, N. Song, W. Shen, M. Allen, M. Javanmard, A ten-minute, single step, label-free, sample-to-answer assay for qualitative detection of cytokines in serum at femtomolar levels. *Biomed. Microdevices* **22**, 73 (2020).
21. P. K. Vabbina, A. Kaushik, N. Pokhrel, S. Bhansali, N. Pala, Electrochemical cortisol immunosensors based on sonochemically synthesized zinc oxide 1D nanorods and 2D nanoflakes. *Biosens. Bioelectron.* **63**, 124–130 (2015).
22. J. Y. Kim, D. A. Fluri, J. M. Kelm, A. Hierlemann, O. Frey, 96-well format-based microfluidic platform for parallel interconnection of multiple multicellular spheroids. *J. Lab. Autom.* **20**, 274–282 (2015).
23. J. Paredes, S. Becerro, F. Arizti, A. Aguinaga, J. L. Del Pozo, S. Arana, Interdigitated microelectrode biosensor for bacterial biofilm growth monitoring by impedance spectroscopy technique in 96-well microtiter plates. *Sens. Actuators B* **178**, 663–670 (2013).
24. C. H. Chuang, M. Shaikh, *Point-of-Care Diagnostics—New Progresses and Perspectives* (2017), IAPC Publishing, Zagreb, Croatia, pp. 171–201.
25. S. K. Arya, P. Zhurauski, P. Jolly, M. R. Batistuti, M. Mulato, P. Estrela, Capacitive aptasensor based on interdigitated electrode for breast cancer detection in undiluted human serum. *Biosens. Bioelectron.* **102**, 106–112 (2018).

26. M. Teke, Ç. Saylkll, Ç. Canbaz, M. K. Sezgintürk, A novel biosensing system using biological receptor for analysis of vascular endothelial growth factor. *Int. J. Pept. Res. Ther.* **20**, 221–230 (2014).
27. Y. Seo, S. Jeong, J. Lee, H. S. Choi, J. Kim, H. Lee, Innovations in biomedical nanoengineering: Nanowell array biosensor. *Nano Converg.* **5**, 9 (2018).
28. P. Kim, B. K. Lee, H. Y. Lee, T. Kawai, K. Y. Suh, Molded nanowell electrodes for site-selective single liposome arrays. *Adv. Mater.* **20**, 31–36 (2008).
29. S. R. Mahmoodi, P. Xie, M. Allen, M. Javanmard, Multiwell plate impedance analysis of a nanowell array sensor for label-free detection of cytokines in mouse serum. *IEEE Sens. Lett.* **4**, 4500104 (2020).
30. J. K. Lee, C. T. Bubar, H. G. Moon, J. Kim, A. Busnaina, H. Y. Lee, S. J. Shefelbine, Measuring bone biomarker alkaline phosphatase with wafer-scale nanowell array electrodes. *ACS Sensors* **3**, 2709–2715 (2018).
31. M. S. Cha, J. K. Lee, S. H. Cho, J. G. Park, H. Y. Lee, S. H. Lim, Y. R. Yoon, Quantitative analysis of H5N1 DNA hybridization on nanowell array electrode. *J. Nanosci. Nanotechnol.* **13**, 5245–5249 (2013).
32. J. Lee, S. Cho, J. Lee, H. Ryu, J. Park, S. Lim, B. Oh, C. Lee, W. Huang, A. Busnaina, H. Lee, Wafer-scale nanowell array patterning based electrochemical impedimetric immunosensor. *J. Biotechnol.* **168**, 584–588 (2013).
33. F. Lisdat, D. Schäfer, The use of electrochemical impedance spectroscopy for biosensing. *Anal. Bioanal. Chem.* **391**, 1555–1567 (2008).
34. S. Li, H. Cui, Q. Yuan, J. Wu, A. Wadhwa, S. Eda, H. Jiang, AC electrokinetics-enhanced capacitive immunosensor for point-of-care serodiagnosis of infectious diseases. *Biosens. Bioelectron.* **51**, 437–443 (2014).
35. X. Liu, K. Yang, A. Wadhwa, S. Eda, S. Li, J. Wu, Development of an AC electrokinetics-based immunoassay system for on-site serodiagnosis of infectious diseases. *Sens. Actuat. A Phys.* **171**, 406–413 (2011).
36. M. S. Mannoor, T. James, D. V. Ivanov, L. Beadling, W. Braunlin, Nanogap dielectric spectroscopy for aptamer-based protein detection. *Biophys. J.* **98**, 724–732 (2010).
37. Z. Ghobaei Namhil, C. Kemp, E. Verrelli, A. Iles, N. Pamme, A. M. Adawi, N. T. Kemp, A label-free aptamer-based nanogap capacitive biosensor with greatly diminished electrode polarization effects. *Phys. Chem. Chem. Phys.* **21**, 681–691 (2019).
38. A. Steensberg, C. P. Fischer, C. Keller, K. Møller, B. K. Pedersen, IL-6 enhances plasma IL-1ra, IL-10, and cortisol in humans. *Am. J. Physiol. Endocrinol. Metab.* **285**, E433–E437 (2003).
39. S. Emaminejad, M. Javanmard, C. Gupta, S. Chang, R. W. Davis, R. T. Howe, Tunable control of antibody immobilization using electric field. *Proc. Natl. Acad. Sci. U.S.A.* **112**, 1995–1999 (2015).
40. Y. Sun, H. Du, C. Feng, Y. Lan, Oriented immobilization of antibody through carbodiimide reaction and controlling electric field. *J. Solid State Electrochem.* **19**, 3035–3043 (2015).
41. J. Suehiro, A. Ohtsubo, T. Hatano, M. Hara, Selective detection of bacteria by a dielectrophoretic impedance measurement method using an antibody-immobilized electrode chip. *Sens. Actuators B* **119**, 319–326 (2006).
42. O. Tabasi, C. Falamaki, Controlled immobilization of IgG1 on carboxymethyl and amino-dextran SPR chips under external vertical electric fields. *Appl. Surf. Sci.* **490**, 251–259 (2019).
43. D. A. Armbruster, T. Pry, Limit of blank, limit of detection and limit of quantitation. *Clin. Biochem. Rev.* **29** (suppl. 1), S49–S52 (2008).
44. A. Makaraviciute, A. Ramanaviciene, Site-directed antibody immobilization techniques for immunosensors. *Biosens. Bioelectron.* **50**, 460–471 (2013).
45. R. D. Munje, S. Muthukumar, A. Panneer Selvam, S. Prasad, Flexible nanoporous tunable electrical double layer biosensors for sweat diagnostics. *Sci. Rep.* **5**, 14586 (2015).
46. R. Massey, S. Bebe, R. Prakash, Aptamer-enhanced organic electrolyte-gated FET biosensor for high-specificity detection of cortisol. *IEEE Sens. Lett.* **4**, 4500604 (2020).
47. A. Kaushik, A. Yndart, R. Dev Jayant, V. Sagar, V. Atluri, S. Bhansali, M. Nair, Electrochemical sensing method for point-of-care cortisol detection in human immunodeficiency virus-infected patients. *Int. J. Nanomed.* **10**, 677–685 (2015).
48. A. Kumar, S. Aravamudhan, M. Gordic, S. Bhansali, S. S. Mohapatra, Ultrasensitive detection of cortisol with enzyme fragment complementation technology using functionalized nanowire. *Biosens. Bioelectron.* **22**, 2138–2144 (2007).
49. A. Vasudev, A. Kaushik, Y. Tomizawa, N. Norena, S. Bhansali, An LTCC-based microfluidic system for label-free, electrochemical detection of cortisol. *Sens. Actuators B* **182**, 139–146 (2013).
50. A. Kaushik, A. Vasudev, S. K. Arya, S. Bhansali, Mediator and label free estimation of stress biomarker using electrophoretically deposited Ag@AgO–polyaniline hybrid nanocomposite. *Biosens. Bioelectron.* **50**, 35–41 (2013).
51. M. Sekar, M. Pandiaraj, S. Bhansali, N. Ponpandian, C. Viswanathan, Carbon fiber based electrochemical sensor for sweat cortisol measurement. *Sci. Rep.* **9**, 403 (2019).
52. M. Ku, J. Kim, J.-E. Won, W. Kang, Y.-G. Park, J. Park, J.-H. Lee, J. Cheon, H. H. Lee, J.-U. Park, Smart, soft contact lens for wireless immunosensing of cortisol. *Sci. Adv.* **6**, eabb2891 (2020).
53. S. K. Tuteja, C. Ormsby, S. Neethirajan, Noninvasive label-free detection of cortisol and lactate using graphene embedded screen-printed electrode. *Nano Micro Lett.* **10**, 41 (2018).
54. S. Sheibani, L. Capua, S. Kamaei, S. S. A. Akbari, J. Zhang, H. Guerin, A. M. Ionescu, Extended gate field-effect-transistor for sensing cortisol stress hormone. *Commun. Mater.* **2**, 10 (2021).
55. K. S. Kim, S. R. Lim, S.-E. Kim, J. Y. Lee, C.-H. Chung, W.-S. Choe, P. J. Yoo, Highly sensitive and selective electrochemical cortisol sensor using bifunctional protein interlayer-modified graphene electrodes. *Sens. Actuators B* **242**, 1121–1128 (2017).
56. N. Dhull, G. Kaur, V. Gupta, M. Tomar, Highly sensitive and non-invasive electrochemical immunosensor for salivary cortisol detection. *Sens. Actuators B* **293**, 281–288 (2019).

Acknowledgments

Funding: This work was sponsored by the Defense Advanced Research Projects Agency (DARPA) Biological Technologies Office (BTO) Electrical Prescriptions (ElectRx) program managed by E. V. Giesen through the DARPA Contracts Management Office Grant/Contract Number HR0011-16-2-0026 and Contract Number N660011824018. The views, opinions, and/or findings expressed are those of the authors and should not be interpreted as representing the official views or policies of the Department of Defense or the U.S. government. The devices were fabricated using tools in the Rutgers Weeks Hall Micro and Nanofabrication Facility, and City University of New York Center for Nanofabrication. **Author contributions:** S.R.M. performed methodology, data curation, conceptualization, writing—original draft, and investigation; P.X. performed methodology and conceptualization; D.P.Z. performed conceptualization, investigation, methodology, and writing—review and editing; E.J.P. performed supervision, conceptualization, and investigation; R.S.G. performed methodology, investigation, and writing—review and editing; C.R.W.K. performed methodology, investigation, and writing—review and editing; H.H.L. performed supervision, conceptualization, funding acquisition, and writing—review and editing; M.G.A. performed supervision, conceptualization, and funding acquisition; and M.J. performed supervision, conceptualization, funding acquisition, and writing—review and editing. **Competing interests:** The authors declare the following financial interests/personal relationships, which may be considered as potential competing interests: P.X., M.J., M.G.A., W. Shen, and N. Song, Rutgers State University of New Jersey, and University of Pennsylvania, 2020. Apparatus and methods for monitoring of biomarkers in blood. U.S. Patent Application 16/852,113; publication no.: US 2020/0261907 A1; publication date: 20 August 2020.] The authors declare no other competing interests. **Data and materials availability:** All data needed to evaluate the conclusions in the paper are present in the paper and/or the Supplementary Materials.

Submitted 28 October 2020
Accepted 18 May 2021
Published 30 June 2021
10.1126/sciadv.abf4401

Citation: S. R. Mahmoodi, P. Xie, D. P. Zachs, E. J. Peterson, R. S. Graham, C. R. W. Kaiser, H. H. Lim, M. G. Allen, M. Javanmard, Single-step label-free nanowell immunoassay accurately quantifies serum stress hormones within minutes. *Sci. Adv.* **7**, eabf4401 (2021).

ScienceAdvances

Single-step label-free nanowell immunoassay accurately quantifies serum stress hormones within minutes

S. Reza MahmoodiPengfei XieDaniel P. ZachsErik J. PetersonRachel S. GrahamClaire R. W. KaiserHubert H. LimMark G. AllenMehdi Javanmard

Sci. Adv., 7 (27), eabf4401. • DOI: 10.1126/sciadv.abf4401

Science Advances (ISSN 2375-2548) is published by the American Association for the Advancement of Science. 1200 New York Avenue NW, Washington, DC 20005. The title *Science Advances* is a registered trademark of AAAS.